A charged black string wormhole with disclinations: Ray and wave optics

F. Ahmed
Department of Physics, The Assam Royal Global University, Guwahati, 781035, Assam, India.
orcid: 0000-0003-2196-9622

A. Bouzenada
Laboratory of Theoretical and Applied Physics, Echahid Cheikh Larbi Tebessi University, 12001, Algeria,
Research Center of Astrophysics and Cosmology, Khazar University, Baku AZ1096, 41 Mehseti Street, Azerbaijan.
orcid: 0000-0002-3363-980X

İ. Sakallı
Physics Department, Eastern Mediterranean University, Famagusta 99628, North Cyprus via Mersin 10, Turkey,
orcid: 0000-0001-7827-9476

Received 29 March 2026; accepted 19 June 2026

This study investigates the optical behavior of photon rays and scalar waves in a three-dimensional static Black String Charged Wormhole (BSCWH) spacetime featuring topological disclinations. By analyzing null geodesics and the scalar Helmholtz equation, we present a unified treatment of light and wave propagation in curved spacetime with geometric defects. The disclination parameter accounts for angular deficits due to topological defects, the wormhole parameter governs throat geometry, and the Neveu-Schwarz (NS) charge introduces a string-inspired field contribution. These factors jointly influence light bending, photon orbits, and scalar wave modes. Scalar wave propagation reduces to a Schrödinger-like equation with an effective potential, from which we derive a spatially and frequency-dependent effective refractive index. We obtain a closed-form weak-field deflection angle in terms of the geometric parameters and the disclination, and demonstrate that the trivial redshift function inherent to the BSCWH geometry precludes the formation of a photon sphere, yielding instead a critical impact parameter set by the throat radius. In the wave-optics sector, we show that the effective potential diverges at the throat, enforcing total reflection of scalar waves and producing frequency-dependent phase shifts characteristic of a dispersive analogue-gravity medium. Our findings reveal how curvature, charge, and topological features modify optical signatures, with implications for gravitational lensing, analogue gravity experiments, and optical media design. This work highlights the role of string-inspired effects and spacetime defects in shaping wave dynamics near wormholes.

Keywords: Geodesic motion; optical propagation; effective refractive index; Helmholtz equation; effective potential; deflection angle; disclination; analogue gravity.

DOI: https://doi.org/10.31349/RevMexFis.72.050802

1. Introduction

Wormholes (WHs) are theoretical solutions to the Einstein Field Equations (EFE), representing bridges that may connect distant regions of the same universe or entirely different universes. Characterized by a finite-radius throat, these structures are sustained by matter-energy configurations that may uphold or violate classical energy conditions. The concept originated with early developments in General Relativity (GR), notably the Einstein-Rosen bridge proposed by Einstein and Rosen as a connection between two asymptotically flat space-times [1, 2]. Subsequent models include the Ellis-Bronnikov solution [3, 4], as well as Reissner-Nordström and Kerr-type WHs, which were later explored in Euclidean contexts [5, 6]. A major advancement came with the Morris-Thorne wormhole (MTW), a static, spherically symmetric solution that requires exotic matter violating the null and weak energy conditions at the throat [7]. To address this, various studies have proposed WH solutions that avoid exotic matter within both standard GR and modified gravity frameworks [10–12]. Additionally, WHs have been examined as potential time machines, where a time shift between the mouths allows for temporal travel [13]. Traversable WHs have also been studied in cosmological settings, including de Sitter and anti-de Sitter space-times [15, 16]. Beyond these static charged configurations, recent work has enlarged the catalogue of exact rotating wormholes. Within Einstein-Maxwell-dilaton (EMD) theory, traversable solutions carrying electric, magnetic, and NS-type charges have been built and shown to keep their ring singularity causally hidden behind the throat, a property named wormhole cosmic censorship [18-21]. Rotating traversable WHs in Einstein-Maxwell theory, together with their NUT-charged generalizations, have further clarified the role of Misner strings and the separation of angular momentum from gravitomagnetic charge in these geometries [22-25].

Black strings (BS) are extended gravitational objects that arise by augmenting higher-dimensional BH solutions [26-35] with additional flat spatial directions. This construction leads to horizon topologies of the form $S^{d-2} \times \mathbb{R}$. A seminal investigation into the stability of these configurations was conducted by Gregory and Laflamme [36,37], who demonstrated that neutral BS in dimensions greater than four are susceptible to a long-wavelength instability. This phenomenon, now known as the Gregory-Laflamme (GL) instability, occurs when perturbation modes along the string direction grow exponentially over time, provided their wavelength exceeds a critical threshold. The standard neutral BS metric is obtained by extending the Schwarzschild-Tangherlini BH solution [38] along an additional spatial dimension that is translationally invariant. These uniform BS solutions possess event horizons that are either infinite or compactified periodically, maintaining translational symmetry along the extended direction. However, the onset of GL instability breaks this symmetry and may lead to a transition toward non-uniform BS [39,40] or localized BH phases. In the context of string theory and supergravity, analogous instabilities have been observed in systems such as near-extremal or smeared $\mathcal{D}$-branes wrapped on transverse circles [41-43]. These scenarios are often connected to neutral Kaluza-Klein BH phases via dualities and Lorentz boosts. An important theoretical development in this area is the Gubser-Mitra conjecture, which postulates a correspondence between thermodynamic and classical (dynamical) instabilities in extended gravitational configurations. This conjecture has been extensively studied in the context of smeared branes, supporting the interpretation of GL-type instabilities as manifestations of underlying thermodynamic instability [41]. Furthermore, phase transitions between BS and BH have been explored within strongly coupled thermal field theories, particularly through holographic duality and compactified supersymmetric Yang-Mills models [42]. These phenomena carry significant implications for braneworld scenarios. In models with large extra dimensions [44,45], or in warped geometries such as those proposed in the Randall-Sundrum framework [46,47], BS solutions are expected to form and exhibit GL-like instabilities, mirroring the behavior observed in higher-dimensional gravitational systems. Thin-shell WHs constructed from charged BS spacetimes [48], as well as embeddings of WHs and dyonic BS in warped braneworlds [49], have further enriched the landscape of extended gravitational objects. Charged BS and black branes have also been studied in higher-curvature Lovelock theories [50], while wave equations governing perturbations of rotating charged BS have been analyzed in Ref. [51]. In the string-theoretic context, massless BH and charged WH solutions have been constructed [52], providing a natural arena for exploring the interplay between gauge fields and topology.

The study of ray and wave optics in curved manifolds provides a powerful framework for understanding how spacetime geometry influences electromagnetic radiation. Within the context of GR, mass and energy curve spacetime, thereby affecting light propagation through phenomena such as gravitational lensing (GL) [53], wave interference patterns [54], and modifications in scattering amplitudes [55]. These effects are particularly evident in features like photon rings observed near compact astrophysical objects [56]. However, direct experimental verification remains difficult due to gravity's inherently weak coupling, requiring astronomical distances for measurable deviations. To address this limitation, analogue gravity systems have been developed to replicate relativistic geometries in controlled laboratory environments [57,58]. These analogues span diverse platforms, including the observation of Hawking-like radiation in Bose-Einstein condensates [59], simulations of relativistic orbits using refractive-index-engineered optical materials [60], and photonic setups that mimic GL [61]. Another complementary approach involves reducing the spatial dimensionality of curved space-times (from $\mathcal{D}$ to $3\mathcal{D}$), thereby facilitating experimental access to curvature-induced wave phenomena [62]. This geometrically inspired modeling approach was significantly advanced by Batz *et al*. [63], whose foundational work established a nonlinear Schrödinger-type framework for describing light propagation on surfaces of constant Gaussian curvature. Their theory deepens the connection between geometry and wave dynamics and has inspired research across classical optics, plasmonics [64], and quantum wave transport [65]. In particular, their model elucidates how curvature directly governs wave evolution in structured optical environments [66,67]. In parallel, the geometrical optics of topological defects such as disclinations has been explored in condensed-matter analogues [68], while surface-plasmon models of BH and WH optics [69] and metamaterial platforms for ray optics [70] have demonstrated that curved-space optical phenomena can be faithfully reproduced in laboratory settings. Classical optics for charged BH spacetimes has also been developed in a rigorous mathematical framework [71], and wave-optics effects in GL of gravitational waves have been probed as signatures of dark-matter substructure [72]. Recent developments in the fields of photonics and quantum physics have led to significant advances in understanding wave propagation and particle interactions in complex media. Dos S. Azevedo *et al.* [73] have demonstrated novel nonlinear optical phenomena in engineered materials, highlighting new avenues for controlling light at the nanoscale. Complementing this, Xu *et al.* [74] analyzed light manipulation techniques within advanced photonic structures, emphasizing applications in optical communication and sensing. Meanwhile, Shao *et al.* [75] provided valuable insights into wave dynamics in disordered systems, revealing mechanisms behind localization and enhanced scattering effects. On a theoretical and fundamental physics level, Dogan *et al.* have made substantial contributions through a series of works [76-78] focusing on quantum field theoretic approaches to particle behavior in curved spacetime and nontrivial geometries, including ray geodesics and wave propagation on WH-like surfaces [79]. Their research sheds light on how topological and geometric effects influence particle spectra and interaction cross-sections, thereby opening new possibilities for exploring physics beyond the Standard Model. Moreover, Ahmed *et al.* [80,81] have advanced the understanding of symmetry-breaking mechanisms and their implications for particle mass generation and vacuum stability. Their investigations provide crucial theoretical foundations that may guide future experimental searches for new physics phenomena. Collectively, these interdisciplinary efforts demonstrate the rich interplay between optical physics and high-energy theory, driving forward the frontier of modern physics.

In this paper, we investigate a three-dimensional static traversable black string charged wormhole (BSCWH) space-time embedded with disclinations. We explore both ray optics and wave optics in this curved space-time background. For ray optics, we analyze null geodesic (NG) motion to determine the behavior of photon trajectories. For wave optics, we examine the scalar Helmholtz equation and, by employing a suitable ansatz for the scalar field, recast it into a Schrödinger-like form. This transformation allows us to identify an effective potential that governs the wave dynamics. From this potential, we derive an effective refractive index (RI) that depends on both spatial coordinate and wave frequency. We demonstrate how geometric parameters, such as the throat radius, the NS charge, the curvature scale, and the disclination affect the photon paths and the RI profile in the WH geometry. In addition, we derive a closed-form weak-field approximation for the deflection angle, identify the critical impact parameter governing photon capture, and present numerical tables that quantify the dependence of key optical observables on the spacetime parameters.

The structure of this paper is as follows: In Sec. 2, we introduce a three-dimensional, static, and circularly symmetric charged BSCWH with disclinations. In Sec. 3, we analyze NG motion and derive the corresponding photon trajectories, including the critical impact parameter and the weak-field deflection angle. Section 4 is devoted to the study of wave optical properties in this curved space-time background, where we obtain an effective RI. Finally, in Sec. 5, we summarize our findings and present concluding remarks. Throughout this work, we adopt natural units where $c = 1 = 8\,\pi\,G = \hbar$.

2. Three-dimensional BSCWH with disclinations

In this section, we introduce the three-dimensional static and circularly symmetric BSCWH with disclinations. In the subsequent sections, we investigate its ray and wave optical properties and analyze how the geometric parameters influence these characteristics.

In Ref. [82], the author proposed 3D traversable WH metric analogue to the MTW 4D case [7,11]. The line element is described by the circular symmetry in the chart (t, r, ϕ) as,

$$ds^2 = -e^{2\,\Phi(r)}\,dt^2 + \frac{dr^2}{1-\frac{b(r)}{r}} + r^2\,d\phi^2, \tag{1}$$

where $\Phi(r)$ is a redshift function and $b(r)$ is a shape function of a traversable WH. The flare-out condition is given by $\left.|r\,b'(r) - b(r)|\right|_{r=r_0} < 0$, while a throat of WH is defined as $b(r = r_0) = r_0$.

In Ref. [83], the authors considered a logarithmic dilaton profile, $\phi = -\ln(r/\ell)$, as the dual of a constant dilaton with a trivial redshift function $\Phi(r) = 0$, and used this to generate a static, circularly symmetric 3D charged BSCWH. By adding suitable matter sources-including the dilaton scalar, they arrived at a line element of the form with disclinations given by

$$ds^2 = -dt^2 + \frac{dr^2}{f(r)} + \alpha^2\,r^2\,d\phi^2, \tag{2}$$

where the metric function $f(r)$ is given by

$$f(r) = 1 - b(r)/r, \qquad b(r) = b_0 - \frac{\mathcal{Q}^2\,\ell^4}{4\,r}. \tag{3}$$

For completeness, we recall the theory that produces the line element (2). It descends from the three-dimensional low-energy effective action of string theory [83], which in the string frame reads

$$S = \frac{1}{2}\int d^3x\,\sqrt{-g}\,e^{-2\,\varphi}\Bigg[R + 4\,(\nabla\varphi)^2 + \frac{4}{\ell^2} - \frac{1}{12}\,H_{\mu\nu\rho}\,H^{\mu\nu\rho}\Bigg], \tag{4}$$

with φ the dilaton (distinct from the redshift function Φ), ℓ the curvature (string) length, and $H_{\mu\nu\rho} = \partial_{[\mu}B_{\nu\rho]}$ the NS three-form field strength. In three dimensions the antisymmetric three-form must be proportional to the Levi-Civita tensor, $H_{\mu\nu\rho} = \mathcal{Q}\,\sqrt{-g}\,\epsilon_{\mu\nu\rho}$, so the whole NS sector enters through the single charge $\mathcal{Q}$. Taking the logarithmic dilaton $\varphi = -\ln(r/\ell)$ of Ref. . [83], dual to a constant dilaton with trivial redshift $\Phi(r) = 0$, the field equations return the shape function already quoted in Eq. (3).

It helps to read the matter content straight off the geometry. In the Einstein frame the line element (2) solves $G_{\mu\nu} = T^{\rm eff}_{\mu\nu}$ in the units $8\,\pi\,G = 1$ used here. A short calculation leaves a single non-vanishing mixed component,

$$G^t{}_t = \frac{f'(r)}{2\,r}, \qquad G^r{}_r = G^\phi{}_\phi = 0, \tag{5}$$

so the effective source is an energy density with no radial or tangential pressure,

$$\rho = -\frac{f'(r)}{2\,r} = -\frac{b_0}{2\,r^3} + \frac{\mathcal{Q}^2\,\ell^4}{4\,r^4}, \qquad p_r = p_\phi = 0. \tag{6}$$

Because r_0 is a simple (non-extremal) throat, $f(r_0) = 0$ with $f'(r_0) > 0$, and hence $\rho(r_0) < 0$. The energy density turns negative near the throat. This is the expected signature of the null energy condition violation that keeps the wormhole open, with the dilaton and NS matter of the action (4) supplying the exotic source. Here, α denotes the disclination parameter [84-86], which characterizes the angular deficit caused by topological defects in the space-time. The parameter ℓ represents the curvature radius, serving as a fundamental length scale in the geometry. The quantity $\mathcal{Q}$ corresponds to the NS (Neveu-Schwarz) charge, associated with the antisymmetric tensor field arising in the NS sector of string theory. Finally, b_0 is an integration constant, often related to the WH throat or initial geometric conditions. It is worth noting that the metric function $f(r) = \big(1 - [b_0/r] + [\mathcal{Q}^2\,\ell^4/4\,r^2]\big)$ satisfies $f(r) \to 1$ as $r \to \infty$, indicating that the space-time becomes asymptotically conical. This behavior, rather than asymptotic flatness, arises due to the presence of disclinations encoded by the parameter α.

The metric tensor $g_{\mu\nu}$ and its inverse $g^{\mu\nu}$ for the space-time (2) are given by

$$g_{\mu\nu} = \text{diag}\left(-1,\, \frac{1}{f(r)},\, \alpha^2\, r^2\right), \tag{7}$$

$$g^{\mu\nu} = \text{diag}\left(-1,\, f(r),\, \frac{1}{\alpha^2\, r^2}\right). \tag{8}$$

The throat radius of the WH is obtained by the following condition:

$$f(r = r_0) = 0. \tag{9}$$

Using the relation (3), we find the throat radius as,

$$r_0 = b_0/2 + \sqrt{b_0^2 - \mathcal{Q}^2\,\ell^4}/2 \geq b_0/2, \tag{10}$$

provided the constraint on the parameters satisfied $b_0 \geq \mathcal{Q}\,\ell^2$. The range of the NS charge is $\mathcal{Q} \in (0, b_0/\ell^2]$.

TABLE I. Throat radius r_0 for various values of b_0 and $\mathcal{Q}$ with $\ell = 1$. The constraint $b_0 \geq \mathcal{Q}\,\ell^2$ must be satisfied.

b_0	$\mathcal{Q}$	r_0
1.0	0.2	0.989898
1.0	0.4	0.958258
1.0	0.6	0.900000
1.0	0.8	0.800000
1.0	1.0	0.500000
1.5	0.2	1.493303
1.5	0.4	1.472842
1.5	0.6	1.437386
1.5	0.8	1.384429
1.5	1.0	1.309017
2.0	0.2	1.994987
2.0	0.4	1.979796
2.0	0.6	1.953939
2.0	0.8	1.916515
2.0	1.0	1.866025
2.5	0.2	2.495994
2.5	0.4	2.483896
2.5	0.6	2.463466
2.5	0.8	2.434272
2.5	1.0	2.395644

The flare-out condition at the throat requires $b'(r_0) < 1$. From Eq. (3), we compute $b'(r) = \mathcal{Q}^2\,\ell^4/(4\,r^2)$, which gives

$$b'(r_0) = \frac{\mathcal{Q}^2\,\ell^4}{4\,r_0^2}. \tag{11}$$

Since $r_0 \geq b_0/2 \geq \mathcal{Q}\,\ell^2/2$, we have $4\,r_0^2 \geq \mathcal{Q}^2\,\ell^4$, ensuring $b'(r_0) \leq 1$, with equality only in the extremal limit $b_0 = \mathcal{Q}\,\ell^2$. Thus, the flare-out condition is satisfied for all non-extremal parameter choices.

As seen from the table, the throat radius r_0 decreases monotonically with increasing NS charge $\mathcal{Q}$ for fixed b_0, and collapses to the extremal value $r_0 = b_0/2$ when $b_0 = \mathcal{Q}\,\ell^2$.

3. Ray optics in BSCWH with disclinations

In this section, we analyze NG motion to determine the behavior of photon trajectories in a 3D BSCWH space-time, described by the line element (2). We show geometrical parameters including disclination alter these trajectories.

The NG motion can be studied using a well-known method called the Lagrangian formalism, where the Lagrangian density function is given by $\mathcal{L} = (1/2)\, g_{\mu\nu}\, \dot{x}^\mu\, \dot{x}^\nu$, with the dot denoting differentiation with respect to an affine parameter and $g_{\mu\nu}$ is the metric tensor for curved geometry.

For the metric given in Eq. (2), the Lagrangian density function is given by

$$\mathcal{L} = \frac{1}{2}\left[-\left(\frac{dt}{d\tau}\right)^2 + \frac{1}{f(r)}\left(\frac{dr}{d\tau}\right)^2 + \alpha^2\, r^2\left(\frac{d\phi}{d\tau}\right)^2\right]. \tag{12}$$

From the above function, one can see that there exist two Killing vector fields, namely, $\xi_{(t)} \equiv \partial_t$ associated with temporal coordinate and $\xi_{(\phi)} \equiv \partial_\phi$ associated with the orbital coordinate. The conserved quantities are the energy E and the angular momentum L, fixed by $\mathrm{E} = -g_{\mu\nu}\, \xi^\mu_{(t)}\, \dot{x}^\nu$ and $\mathrm{L} = g_{\mu\nu}\, \xi^\mu_{(\phi)}\, \dot{x}^\nu$. Since $g_{tt} = -1$ and $g_{\phi\phi} = \alpha^2\, r^2$, we find [87]:

$$\mathrm{E} = \frac{dt}{d\tau} \quad , \quad \mathrm{L} = \alpha^2\, r^2\, \frac{d\phi}{d\tau}. \tag{13}$$

The factor α^2 follows directly from $g_{\phi\phi} = \alpha^2\, r^2$, since L is the conserved charge of $\xi_{(\phi)} = \partial_\phi$, that is $\mathrm{L} = g_{\phi\phi}\, \dot{\phi}$. With these, the non-radial NG paths for r coordinate from Eq. (12) simplify to:

$$\frac{1}{f(r)}\left(\frac{dr}{d\tau}\right)^2 = \mathrm{E}^2 - \frac{\mathrm{L}^2}{\alpha^2\, r^2}. \tag{14}$$

The equation of orbit is therefore defined by

$$\left(\frac{1}{r^2}\frac{dr}{d\phi}\right)^2 = \alpha^2\, f(r)\left(\frac{1}{\beta^2} - \frac{1}{r^2}\right), \tag{15}$$

where $\beta = \mathrm{L}/(\alpha\,\mathrm{E})$ is the impact parameter for photon particles, so that the corrected definitions leave Eq. (15) and every expression derived from it unchanged.

3.1. Absence of photon sphere and critical impact parameter

A distinctive feature of the BSCWH geometry (2) is the trivial redshift function $\Phi(r) = 0$, which implies $g_{tt} = -1$. In standard BH spacetimes, the photon sphere (unstable circular photon orbit) arises from the competition between the gravitational redshift (encoded in g_{tt}) and the centrifugal barrier. The effective potential governing photon orbits takes the general form $V_{\rm eff}^{\rm orb}(r) = -g_{tt}(r)/r^2$, whose local maximum defines the photon sphere radius $r_{\rm ps}$.

In the present BSCWH geometry, however, the NG condition (14) can be recast as

$$\dot{r}^2 = f(r)\left(\mathrm{E}^2 - \frac{\mathrm{L}^2}{\alpha^2\, r^2}\right). \tag{16}$$

Defining the orbital effective potential $\mathcal{V}(r) \equiv 1/r^2$, the turning point condition $\dot{r} = 0$ (with $f(r) > 0$) yields

$$\frac{1}{\beta^2} = \frac{1}{r_{\rm tp}^2} \quad \Longrightarrow \quad r_{\rm tp} = \beta. \tag{17}$$

Since $\mathcal{V}(r) = 1/r^2$ is a monotonically decreasing function with no local maximum for finite r, the BSCWH geometry admits *no photon sphere*. This is a direct consequence of $g_{tt} = -1$; in the absence of gravitational redshift, there is no competing radial force to create an unstable circular orbit.

Consequently, the photon dynamics are governed solely by the impact parameter β relative to the throat radius r_0:

- If $\beta > r_0$: the photon reaches the turning point at $r_{\rm tp} = \beta > r_0$, scatters, and returns to infinity. The deflection angle is finite and depends on the spacetime parameters.
- If $\beta = r_0$: the photon grazes the WH throat, defining the **critical impact parameter**

$$\beta_c = r_0 = \frac{b_0}{2} + \frac{\sqrt{b_0^2 - \mathcal{Q}^2\,\ell^4}}{2}. \tag{18}$$

- If $\beta < r_0$: the turning point lies at $r_{\rm tp} = \beta < r_0$, which falls inside the throat region where $f(r) < 0$. The photon reaches the throat and traverses the WH to the other asymptotic region.

The critical impact parameter β_c thus plays the role analogous to the shadow radius in BH spacetimes, delineating scattered from captured (traversing) photon trajectories. Table II presents values of β_c for representative parameter combinations.

Transforming to a new variable via $r = 1/u$ in the above Eq. (15) yields:

$$\left(\frac{du}{d\phi}\right)^2 = \frac{\alpha^2}{\beta^2}\, f(u) - \alpha^2\, u^2\, f(u). \tag{19}$$

where $f(u)$ explicitly can be written as

$$f(u) = 1 - b_0\, u + \frac{\mathcal{Q}^2\,\ell^4}{4}\, u^2. \tag{20}$$

TABLE II. Critical impact parameter $\beta_c = r_0$ and the flare-out derivative $b'(r_0) = \mathcal{Q}^2\ell^4/(4\,r_0^2)$ for various parameter values with $\ell = 1$.

b_0	$\mathcal{Q}$	$\beta_c = r_0$	$b'(r_0)$
1.0	0.2	0.989898	0.010205
1.0	0.4	0.958258	0.043559
1.0	0.6	0.900000	0.111111
1.0	0.8	0.800000	0.250000
1.0	1.0	0.500000	1.000000
1.5	0.4	1.472842	0.018437
1.5	0.6	1.437386	0.043562
1.5	0.8	1.384429	0.083478
1.5	1.0	1.309017	0.145898
2.0	0.4	1.979796	0.010205
2.0	0.6	1.953939	0.023573
2.0	0.8	1.916515	0.043559
2.0	1.0	1.866025	0.071798

Differentiating both sides of Eq. (19) w. r. t. ϕ and after simplification results

$$\frac{d^2u}{d\phi^2} + \alpha^2\left(1 - \frac{\mathcal{Q}^2\,\ell^4}{4\,\beta^2}\right) u = -\frac{\alpha^2\, b_0}{2\,\beta^2} + \frac{3\,\alpha^2\, b_0}{2}\, u^2 - \frac{\alpha^2\,\mathcal{Q}^2\,\ell^4}{2} u^3. \tag{21}$$

In the limit $\mathcal{Q} = 0$ corresponding to the absence of NS charge, the above equation reduces as

$$\frac{d^2u}{d\phi^2} + \alpha^2\, u + \frac{\alpha^2\, b_0}{2\,\beta^2} = \frac{3}{2}\,\alpha^2\, b_0\, u^2. \tag{22}$$

Figures 1–2 and 3–4 present the parametric plots of photon trajectories $r(\varphi) = 1/u(\varphi)$ based on Eq. (21) for various values of the disclination parameter α and the NS charge $\mathcal{Q}$. Figure 5 compares the photon trajectories with and without the influence of α and $\mathcal{Q}$, highlighting the impact of these parameters on the photon's path. We set the initial boundary condition $u(0) = 0.001$ and $u'(0) = 0.01$.

Moreover, for radial NG, where the angular momentum vanishes, $\mathrm{L} = 0$, the geodesic paths for t and r coordinates from Eqs. (13)-(14) reduces as,

$$\frac{dt}{d\tau} = \mathrm{E}, \quad \frac{dr}{d\tau} = \pm\,\mathrm{E}\,\sqrt{f(r)}. \tag{23}$$

From the above equation, we find the radial motion of photon particles in temporal coordinate as,

$$\frac{dr}{dt} = \pm, \sqrt{f(r)}. \tag{24}$$

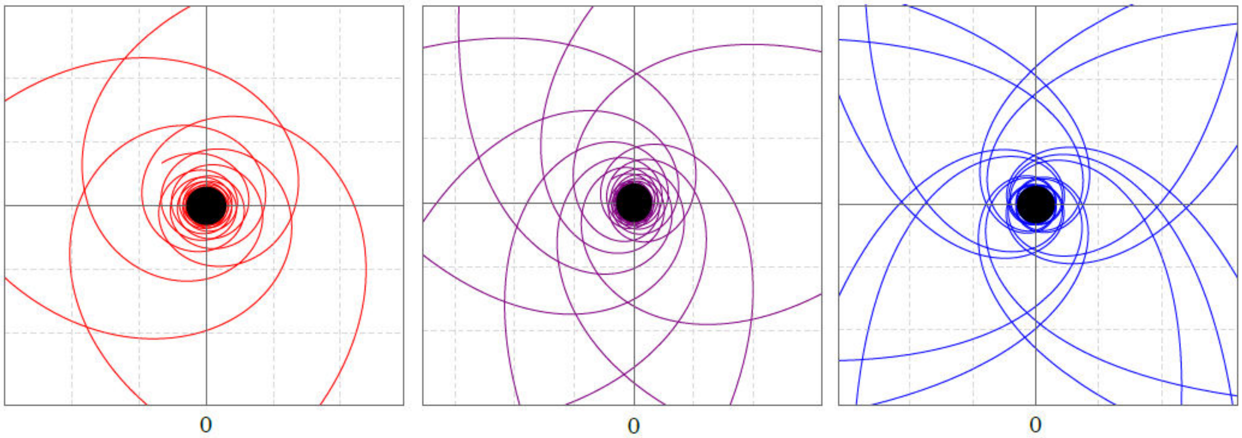

(i) $\alpha = 0.1$ (ii) $\alpha = 0.2$ (iii) $\alpha = 0.3$

FIGURE 1. Parametric plot of the Photon trajectory for different values of the disclination parameter α, while keeping $\beta = 1.5,\ \mathcal{Q} = 1 = \ell = b_0$. The horizontal and vertical axes are the Cartesian coordinates $X = r\cos\phi$ and $Y = r\sin\phi$ (in units of b_0) built from the orbit $r(\phi) = 1/u(\phi)$ of Eq. (21); the central black disk marks the throat at $r = r_0$.

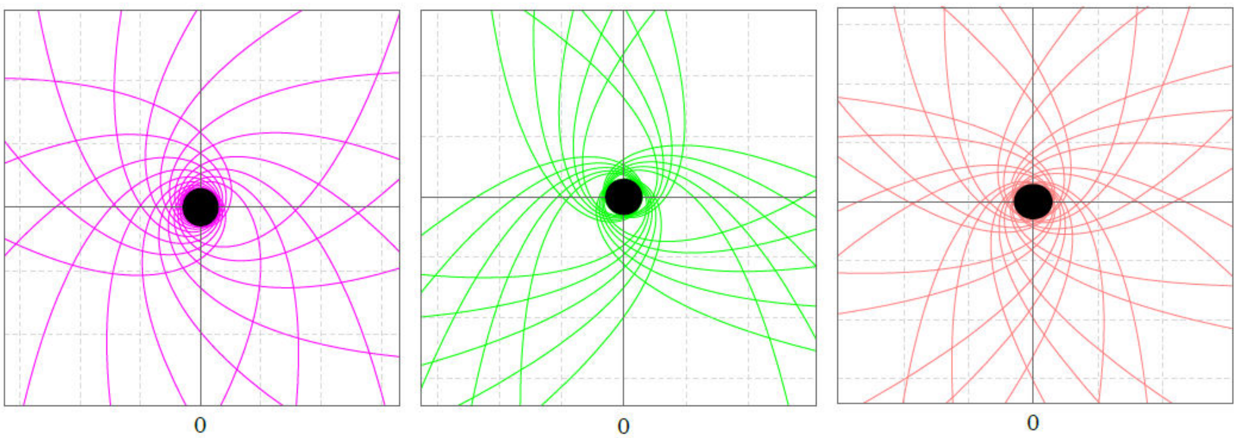

(iv) $\alpha = 0.4$ (v) $\alpha = 0.5$ (vi) $\alpha = 0.6$

FIGURE 2. Parametric plot of the Photon trajectory for different values of the disclination parameter α, while keeping $\beta = 1.5,\ \mathcal{Q} = 1 = \ell = b_0$. The horizontal and vertical axes are the Cartesian coordinates $X = r\cos\phi$ and $Y = r\sin\phi$ (in units of b_0) built from the orbit $r(\phi) = 1/u(\phi)$ of Eq. (21); the central black disk marks the throat at $r = r_0$.

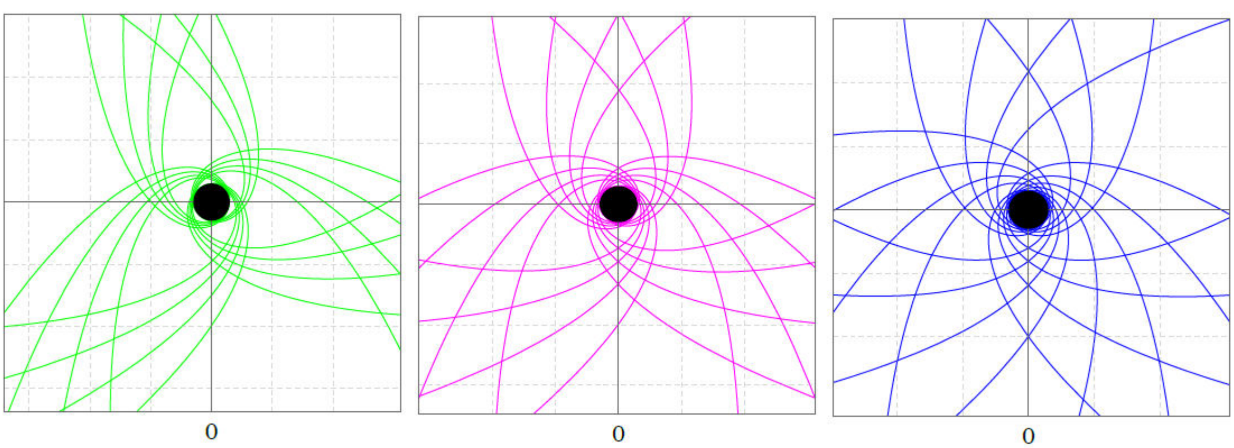

(i) $\mathcal{Q} = 0.2$ (ii) $\mathcal{Q} = 0.4$ (iii) $\mathcal{Q} = 0.6$

FIGURE 3. Parametric plot of the Photon trajectory for different values of NS charge $\mathcal{Q}$, while keeping $\beta = 1.5,\ \alpha = 0.5,\ \ell = 1 = b_0$. The axes are the Cartesian coordinates $X = r\cos\phi$ and $Y = r\sin\phi$ (in units of b_0) obtained from the orbit $r(\phi) = 1/u(\phi)$; the central black disk marks the throat at $r = r_0$.

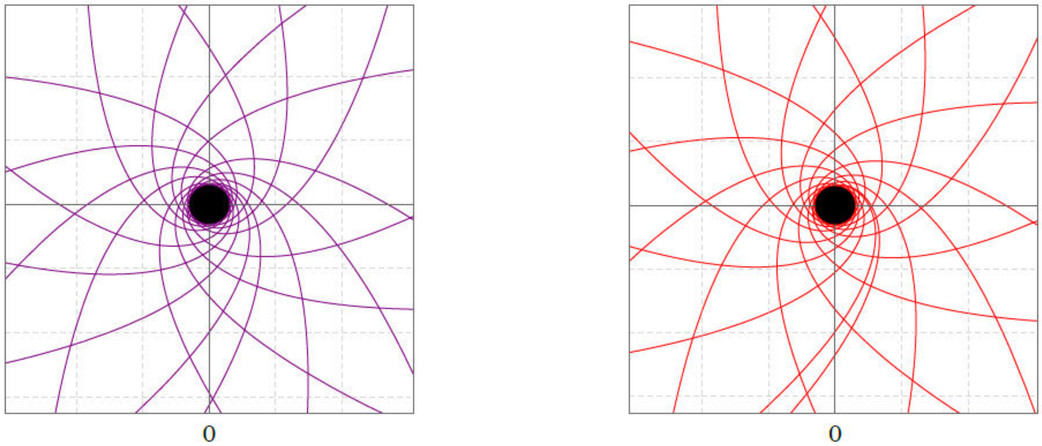

(iv) $\mathcal{Q} = 0.8$ (v) $\mathcal{Q} = 1.0$

FIGURE 4. Parametric plot of the Photon trajectory for different values of NS charge $\mathcal{Q}$, while keeping $\beta = 1.5$, $\alpha = 0.5$, $\ell = 1 = b_0$. The axes are the Cartesian coordinates $X = r\cos\phi$ and $Y = r\sin\phi$ (in units of b_0) obtained from the orbit $r(\phi) = 1/u(\phi)$; the central black disk marks the throat at $r = r_0$.

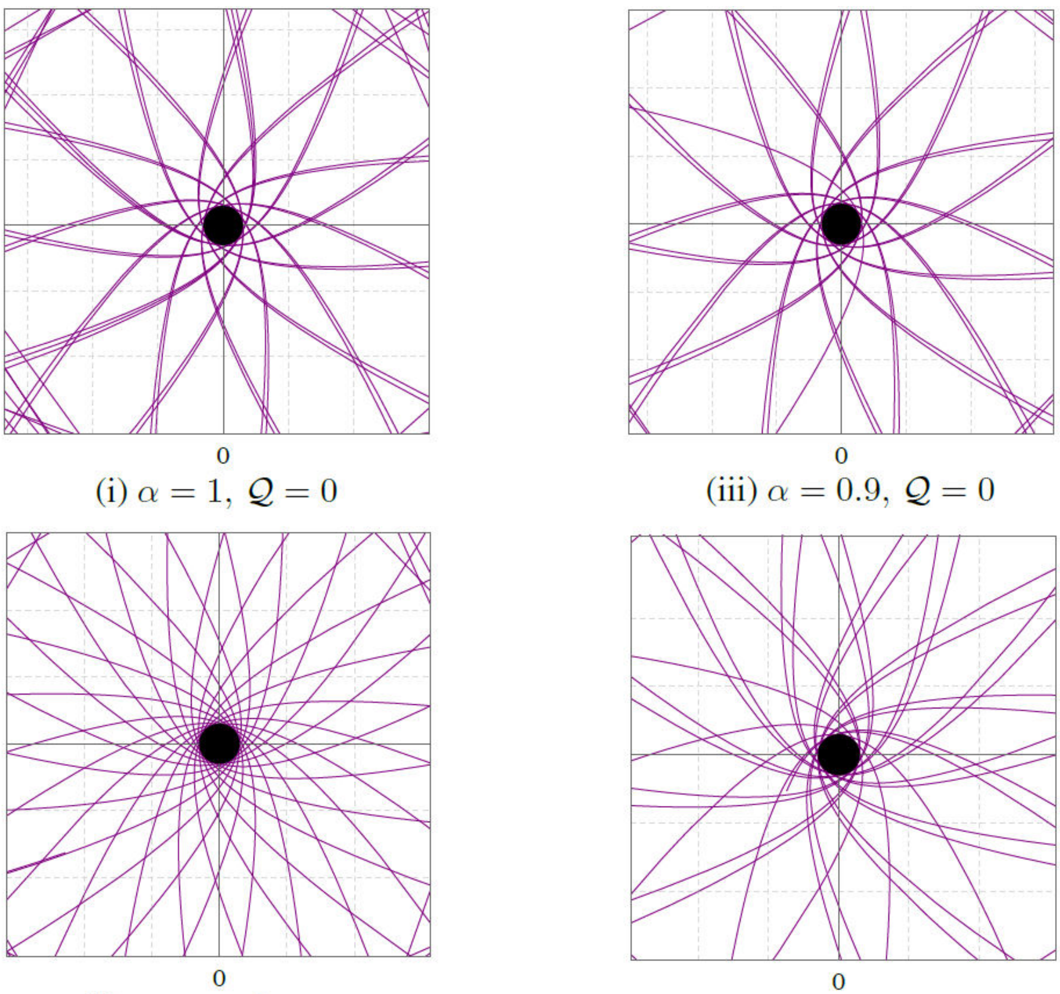

(i) $\alpha = 1,\ \mathcal{Q} = 0$ (iii) $\alpha = 0.9,\ \mathcal{Q} = 0$

(ii) $\alpha = 1,\ \mathcal{Q} = 0.9$ (iv) $\alpha = 0.9,\ \mathcal{Q} = 0.9$

FIGURE 5. Parametric plot of the Photon trajectory $r(\phi) = 1/u(\phi)$ for different values of NS charge $\mathcal{Q}$ without and with disclination parameter α, while keeping $\beta = 1.5$, $\ell = 1 = b_0$. The axes are the Cartesian coordinates $X = r\cos\phi$ and $Y = r\sin\phi$ (in units of b_0); the central black disk marks the throat at $r = r_0$.

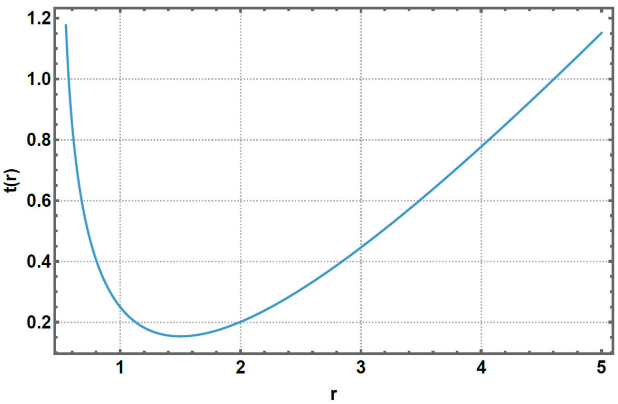

FIGURE 6. Variation of the temporal coordinate $t(r)$ as a function of r for the radial NG motion. Here, we set $\ell = 1, \mathcal{Q} = 1, b_0 = 1, C = 0$. The horizontal axis is the radial coordinate r and the vertical axis is the coordinate time $t(r)$, both in units of b_0.

Therefore, the temporal coordinate $t(r)$ as

$$t(r) = \pm \int \frac{dr}{\sqrt{f(r)}} = \pm \frac{dr}{\sqrt{1 - \frac{b_0}{r} + \frac{\mathcal{Q}^2\,\ell^4}{4\,r^2}}}. \tag{25}$$

Simplification of the above integral results

$$t(r) = \frac{1}{2}\sqrt{r^2 - b_0\,r + \frac{\mathcal{Q}^2\,\ell^4}{4}} - \frac{b_0}{2}\ln\left|r - \frac{b_0}{2} + \sqrt{r^2 - b_0\,r + \frac{\mathcal{Q}^2\,\ell^4}{4}}\right| + C, \tag{26}$$

where C is an integrating constant.

Figure 6 illustrates the evolution of the temporal coordinate $t(r)$ along a radial photon trajectory, plotted as a function of the axial coordinate r. This behavior is obtained by integrating the geodesic equation for radial null trajectories (L $= 0$). In this plot, the curvature radius is set to $\ell = 1$, the NS charge $\mathcal{Q} = 1$, the throat radius $b_0 = 1$, and the integration constant $C = 0$. The curve exhibits a monotonic increase in $t(r)$, with the steepness of the curve reflecting how the space-time geometry causes a delay in coordinate time as the photon approaches the WH throat. Notably, the presence of the charge parameter and the WH geometry both influence the shape of this function through the metric component $f(r)$, thereby affecting the effective gravitational time delay experienced by radially in-falling photons.

To obtain an expression of the deflection angle of photon particles, we can write Eq. (19) with the help of Eq. (20) as,

$$\frac{du}{d\phi} = \frac{\alpha}{\beta}\sqrt{\left(1 - b_0\,u + \frac{\mathcal{Q}^2\,\ell^4}{4}\,u^2\right)\,(1 - \beta^2\,u^2)}. \tag{27}$$

The deflection angle is given by

$$\delta\phi = \frac{\beta}{\alpha}\,\Delta\phi - \pi, \tag{28}$$

where

$$\Delta\phi = \int_{u_0}^{\infty} \frac{du}{\sqrt{\left(1 - b_0\,u + \frac{\mathcal{Q}^2\,\ell^4}{4}\,u^2\right)\,(1 - \beta^2\,u^2)}}. \tag{29}$$

Recall that $u_0 = 1/r_0$, where r_0 is defined in Eq. (10). Noting that for the special case $b_0 = \mathcal{Q}\,\ell^2$, we have $r_0 = b_0/2$, which implies $u_0 = 2/b_0$. Under this condition, the lower limit of the integral in Eq. (29) coincides with the point where the integrand becomes singular. As a result, the integral diverges at the lower limit. We therefore conclude that the deflection angle can be determined only when $b_0 \neq \mathcal{Q}\,\ell^2$.

The integral (29) after a few mathematical steps, we find (see notes at the end)

$$\Delta\phi = \frac{1}{\sqrt{-\beta^2 + \frac{\mathcal{Q}^2\,\ell^4}{4}}}\left[F(\pi/2, k) - F(\phi_0, k)\right] = \frac{1}{\sqrt{-\beta^2 + \frac{\mathcal{Q}^2\,\ell^4}{4}}}\left[K(k) - F(\phi_0, k)\right], \tag{30}$$

where we have defined the following:

$$k^2 = \frac{-\beta^2 - \frac{\mathcal{Q}^2\,\ell^4}{4} + \sqrt{\left(-\beta^2 - \frac{\mathcal{Q}^2\,\ell^4}{4}\right)^2 + b_0^2\,\beta^4}}{2\left(-\beta^2 + \frac{\mathcal{Q}^2\,\ell^4}{4}\right)},$$

$$\phi_0 = \arcsin\left(\sqrt{\frac{\left(-\beta^2 + \frac{\mathcal{Q}^2\,\ell^4}{4}\right)\,(u_0 - \xi_1)}{\left(-\beta^2 - \frac{\mathcal{Q}^2\,\ell^4}{4} + \Sigma\right)\,(u_0 - \xi_2)}}\right),$$

$$u_0 = \frac{2}{b_0 + \sqrt{b_0^2 - \mathcal{Q}^2\,\ell^4}},$$

$$\xi_{1,2} = \frac{b_0 \pm \sqrt{b_0^2 - \mathcal{Q}^2\,\ell^4}}{\frac{1}{2}\,\mathcal{Q}^2\,\ell^4},$$

$$\Sigma = \sqrt{\left(-\beta^2 - \frac{\mathcal{Q}^2\,\ell^4}{4}\right)^2 + b_0^2\,\beta^4}. \tag{31}$$

Here, $K(k)$ and $F(\phi_0, k)$ denote the complete and incomplete elliptic integrals of the first kind, respectively [88,89].

We observe from the above analysis that the deflection angle of photon particles is influenced by geometrical parameters $(b_0, \mathcal{Q}, \ell)$ and the disclinations parameter α.

3.2. Weak-field deflection angle

In the weak-field regime, corresponding to a large impact parameter $\beta \gg b_0$, we can derive a closed-form approximation for the deflection angle by expanding the orbit equation perturbatively. The total angular sweep of a photon traveling from infinity to the turning point $r_{\rm tp} = \beta$ and back is

$$\phi_{\rm total} = \frac{2}{\alpha}\int_0^{1/\beta} \frac{du}{\sqrt{f(u)\,(1/\beta^2 - u^2)}}. \tag{32}$$

Expanding $1/\sqrt{f(u)}$ for small u (*i.e.*, large r),

$$\frac{1}{\sqrt{f(u)}} \approx 1 + \frac{b_0}{2}\,u + \left(\frac{3\,b_0^2}{8} - \frac{\mathcal{Q}^2\,\ell^4}{8}\right)u^2 + \mathcal{O}(u^3), \tag{33}$$

TABLE III. Weak-field deflection angle $\delta\phi_{\rm weak}$ (in radians) for $b_0 = 1$, $\ell = 1$, and selected values of α, $\mathcal{Q}$, and β.

α	$\mathcal{Q}$	β	$\delta\phi_{\rm weak}$
0.7	0.0	5.0	1.665771
0.7	0.5	5.0	1.662966
0.7	1.0	5.0	1.654551
0.8	0.0	5.0	1.064851
0.8	0.5	5.0	1.062396
0.8	1.0	5.0	1.055033
0.9	0.0	5.0	0.597468
0.9	0.5	5.0	0.595286
0.9	1.0	5.0	0.588741
1.0	0.0	5.0	0.223562
1.0	0.5	5.0	0.221598
1.0	1.0	5.0	0.215708
1.0	0.0	10.0	0.105890
1.0	0.5	10.0	0.105400
1.0	1.0	10.0	0.103927
1.0	0.0	20.0	0.051473
1.0	0.5	20.0	0.051350
1.0	1.0	20.0	0.050982

and employing the standard integrals

$$\int_0^{1/\beta} \frac{du}{\sqrt{1/\beta^2 - u^2}} = \frac{\pi}{2},$$
$$\int_0^{1/\beta} \frac{u\,du}{\sqrt{1/\beta^2 - u^2}} = \frac{1}{\beta},$$
$$\int_0^{1/\beta} \frac{u^2\,du}{\sqrt{1/\beta^2 - u^2}} = \frac{\pi}{4\,\beta^2}, \tag{34}$$

we obtain

$$\phi_{\rm total} = \frac{\pi}{\alpha} + \frac{b_0}{\alpha\,\beta} + \frac{\pi\,(3\,b_0^2 - \mathcal{Q}^2\,\ell^4)}{16\,\alpha\,\beta^2} + \mathcal{O}(\beta^{-3}). \tag{35}$$

The weak-field deflection angle is therefore

$$\delta\phi_{\rm weak} = \frac{\pi\,(1-\alpha)}{\alpha} + \frac{b_0}{\alpha\,\beta} + \frac{\pi\,(3\,b_0^2 - \mathcal{Q}^2\,\ell^4)}{16\,\alpha\,\beta^2} + \mathcal{O}(\beta^{-3}). \tag{36}$$

This expression admits a transparent physical interpretation:

1. The first term $\pi(1-\alpha)/\alpha$ represents the **topological deflection** due to the disclination-induced angular deficit. For $\alpha < 1$, this yields a positive deflection, focusing light toward the defect core, in complete analogy with cosmic string lensing [84].
2. The second term $b_0/(\alpha\,\beta)$ is the **leading gravitational deflection**, the $(2+1)$-dimensional analogue of the Schwarzschild result $4M/b$ in four dimensions. It is enhanced by the factor $1/\alpha$ due to the conical geometry.
3. The third term introduces **post-leading corrections** involving both the WH parameter b_0 and the NS charge $\mathcal{Q}$. Notably, the NS charge reduces the deflection angle, counteracting the gravitational bending.

In Table III, we present the weak-field deflection angle $\delta\phi_{\rm weak}$ for representative parameter values, demonstrating the interplay between disclination, gravitational, and charge contributions.

As evident from the table, the disclination parameter α dominates the deflection for moderate impact parameters, while the NS charge provides a secondary correction that systematically reduces $\delta\phi$.

4. Wave optics in BSCWH with disclinations

In this section, we examine the dynamics of wave propagation within the effective geometry of a WH, focusing specifically on the corresponding electromagnetic wave modes. In free space, Maxwell's equations govern the behavior of electromagnetic fields. For a monochromatic wave with time dependence of the form $e^{-i\omega t}$, Maxwell's equations reduce to the Helmholtz equation: $\nabla^2\psi + k^2\psi = 0$, where $k = \omega/c$ is the wave number. This equation describes the spatial distribution of electromagnetic waves under time-harmonic conditions in a source-free region. The solutions to the Helmholtz equation correspond to the permitted electromagnetic modes in the frequency domain.

In the context of curved spacetime or effective geometries such as that of a WH as described by the line element (2), the Helmholtz wave equation can be expressed as [63,67,73-78,80,81]:

$$(\Delta_{\rm LB} + k_g^2)\Psi = 0, \tag{37}$$

where $\Delta_{\rm LB}$ represents the Laplace-Beltrami (LB) operator. The term k_g corresponds to the propagation constant associated with the wave frequency $k_g = \omega/c = \omega$, while $\Delta_{\rm LB}$ shows the effects of curvature on wave propagation. Specifically, for a generic metric $ds^2 = -dt^2 + g_{ij}\,dx^i\,dx^j$, the LB operator takes the following form:

$$\Delta_{\rm LB}\Psi = \frac{1}{\sqrt{g}}\,\partial_i\left(\sqrt{g}\,g^{ij}\partial_j\Psi\right), \tag{38}$$

where $g = \det(g_{ij})$ is the determinant of the spatial metric tensor g_{ij}, and the indices i, j correspond to the coordinates in the geometry, which in this case are r and ϕ. For the metric (2), the determinant of the spatial metric tensor g_{ij} is given by

$$g = \det(g_{ij}) = \frac{\alpha^2\,r^2}{f(r)}. \tag{39}$$

In our case, we find

$$\Delta_{\rm LB}\Psi = \frac{\sqrt{f(r)}}{r}\,\frac{\partial}{\partial r}\left(r\,\sqrt{f(r)}\,\frac{\partial}{\partial r}\right) + \frac{1}{\alpha^2\,r^2}\,\frac{\partial^2}{\partial\phi^2}, \tag{40}$$

To proceed, we now express the Helmholtz equation in a form suitable for the specific geometry of the WH. According to the space-time (2), let us consider the wave function

$$\Psi = \exp(i\,m\,\phi)\,\psi(r), \tag{41}$$

where m is the magnetic quantum number and $\psi(r)$ is the radial function.

Substituting Eq. (40) into Eq. (37) and using the wave function ansatz (41), we arrive at the following equation:

$$\frac{\sqrt{f(r)}}{r}\frac{\partial}{\partial r}\left(r\sqrt{f(r)}\,\frac{\partial\psi}{\partial r}\right) + \left(\omega^2 - \frac{m^2}{\alpha^2\,r^2}\right)\psi(r) = 0. \tag{42}$$

Now, let us try to determine the effective potential acting on waves within the curved background. To do this, we remove the first-order derivative term appeared in the above differential equation. For that, we perform the following transformation:

$$\psi(r) = \frac{\chi(r)}{r^{1/2}\,f(r)^{1/4}}. \tag{43}$$

Substituting this transformation (43) into the Eq. (42) and after simplification results in the Schrödinger-like equation:

$$\chi''(r) + \left(\omega^2 - U(r)\right)\chi(r) = 0, \tag{44}$$

where

$$U(r) = \frac{f''(r)}{4\,f(r)} - \frac{3}{16}\left(\frac{f'(r)}{f(r)}\right)^2 + \frac{f'(r)}{4\,r\,f(r)} + \frac{m^2/\alpha^2 - 1/4}{r^2}. \tag{45}$$

Substituting function $f(r)$ and after simplification results the following expression for the effective potential governing the wave optics as,

$$\begin{aligned} U(r) &= \frac{\mathcal{A}(r)}{\mathcal{D}(r)}, \\ \mathcal{A}(r) &= 2m^2\left(4r^2{+}\mathcal{Q}^2\ell^4\right)^2 + \left(-8r^4{-}8\mathcal{Q}^2r^2\ell^4{+}\mathcal{Q}^4\ell^8\right)\alpha^2 \\ &\quad + 2b_0^2r^2\left(16m^2+\alpha^2\right) - 2b_0r\Big\{8m^2\left(4r^2+\mathcal{Q}^2\ell^4\right) \\ &\quad + \left(-8r^2+\mathcal{Q}^2\ell^4\right)\alpha^2\Big\}, \\ \mathcal{D}(r) &= 2r^2\left(-4b_0r + 4r^2 + \mathcal{Q}^2\ell^4\right)^2\alpha^2. \end{aligned} \tag{46}$$

For the zero magnetic quantum number, $m = 0$, the effective potential reduces as,

$$\begin{aligned} U(r) &= \frac{\mathcal{B}(r)}{\mathcal{D}(r)}, \\ \mathcal{B}(r) &= \left(-8r^4 - 8\mathcal{Q}^2r^2\ell^4 + \mathcal{Q}^4\ell^8\right)\alpha^2 \\ &\quad + 2b_0^2r^2\alpha^2 - 2b_0r\alpha^2\left(-8r^2+\mathcal{Q}^2\ell^4\right). \end{aligned} \tag{47}$$

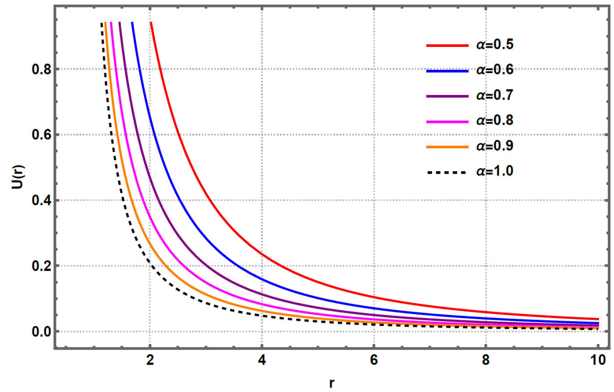

FIGURE 7. Graphical representation of the effective potential $U_{\text{eff}}(r)$ as a function of r for different values of the disclination parameter α. Here, we set $\ell = 1, \mathcal{Q} = 1, b_0 = 1, m = 1$.

The effective potential (46) plays a central role in understanding how wave propagation is influenced by the geometry of the WH. It depends on the radial coordinate r, the magnetic quantum number m, and several geometric parameters, including the throat size b_0, the charge $\mathcal{Q}$, the curvature scale ℓ, and the disclination parameter α. Notably, the WH spacetime induces a repulsive effective potential which acts as a barrier to incoming waves. The strength of this repulsive interaction decreases gradually as the radial distance r increases. As expected from the geometry, the potential diverges in the limit $r \to r_0$, reflecting the strongly repulsive nature near the WH throat for $m = 0$ or $m \neq 0$, and asymptotically vanishes as $r \to \infty$, indicating that spacetime becomes effectively locally flat at large distances.

Figure 7 illustrated the radial variation of the effective potential $U(r)$ for different values of the disclination parameter $\alpha = \{0.7, 0.8, 0.9, 1.0\}$. In this plot, the curvature radius is set to $\ell = 1$, the NS charge $\mathcal{Q} = 1$, the throat radius $b_0 = 1$, and the angular quantum number $m = 1$. As α decreases from unity (implying a stronger angular deficit), the effective potential increases, which physically corresponds to stronger scattering or trapping behavior for scalar waves. This provides us precise information about topological defects in modulating wave dynamics in the WH space-time.

Let us now derive the expression for the RI $n(r,\omega)$. In a spatially varying medium, the Helmholtz equation can be written as $\nabla^2\varphi + k_{\text{eff}}^2(r)\varphi = 0$, where $k_{\text{eff}}(r)$ is the effective wave number that accounts for the influence of the medium on wave propagation. The RI $n(r)$ relates to this effective wave number by $k_{\text{eff}}(r) = (\omega/c)n(r)$. Substituting this relation into the Helmholtz equation yields $\nabla^2\varphi + (\omega/c)^2\,n^2(r)\varphi = 0$, which represents the general form of the wave equation in a medium with a spatially varying RI. Recognizing that the term $k^2 - U_{\text{eff}}(r)$ modifies the system's wave number, and comparing it with the wave equation in the RI medium, we identify $k_{\text{eff}}^2(r) = k^2 - U_{\text{eff}}(r)$. Using the relation $k = \omega/c = \omega$, we obtain $n^2(r) = 1 - [U_{\text{eff}}(r)/\omega^2]$. Therefore, the behavior of the effective potential $U_{\text{eff}}(r)$ directly influences the spatial profile of the RI, which is given by

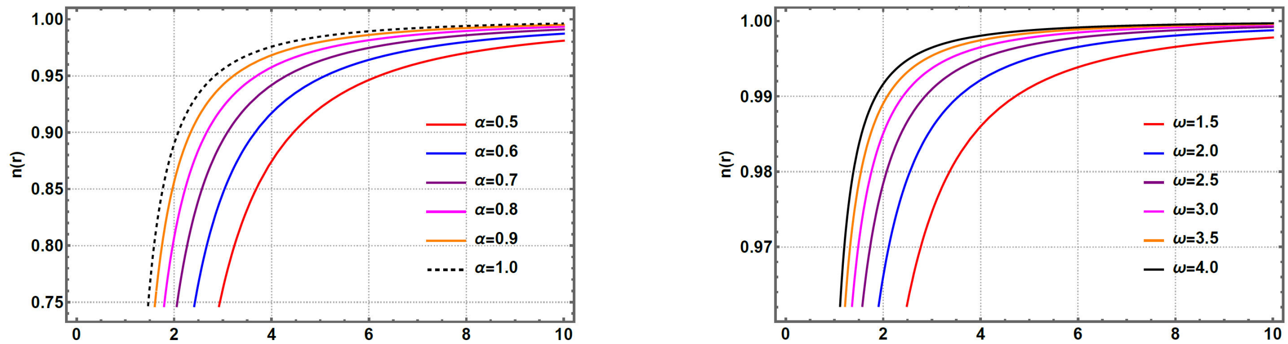

(i) $\omega = 1$ (ii) $\alpha = 0.9$

FIGURE 8. Graphical representation of the effective refractive index $n(r)$ as a function of r for different values of the disclination parameter α (left panel) and frequency ω (right panel). Here, we set $\ell = 1, \mathcal{Q} = 1, b_0 = 1, m = 1$.

$$n(r) = \sqrt{1 - \frac{\mathcal{A}(r)}{\omega^2\,\mathcal{D}(r)}}. \tag{48}$$

For the zero magnetic quantum number, $m = 0$, the RI reduces as,

$$n(r) = \sqrt{1 - \frac{\mathcal{B}(r)}{\omega^2\,\mathcal{D}(r)}}. \tag{49}$$

Figure 8 shows the behavior of the effective RI $n(r)$ as a function of the axial coordinate r, for different values of the disclination parameter α and the wave frequency ω. In the left panel, the frequency is fixed at $\omega = 1$, while in the right panel, the disclination parameter is fixed at $\alpha = 0.9$. Other parameters are held constant across both panels: the curvature radius $\ell = 1$, the NS charge $\mathcal{Q} = 1$, the throat radius $b_0 = 1$, and the angular quantum number $m = 1$. In the left panel, it is observed that as α approaches unity, the RI profile $n(r) < 1$ increases with r. In the right panel, the RI increases with rising wave frequency $\omega = \{1.5, 2.0, 2.5, 3.0\}$, for fixed $\alpha = 0.9$ again $n(r) < 1$. This illustrates a dispersive effect in the WH geometry: higher-frequency waves experience stronger refractive behavior and are more significantly influenced by the curvature and topological defects of the space-time.

A RI $n < 1$ implies that the phase velocity of light or waves in the medium exceeds the speed of light in vacuum, c. This property is characteristic of metamaterials-artificially engineered materials designed to exhibit unusual optical behaviors such as negative refraction, where light bends in the opposite direction compared to conventional materials. Metamaterials with $n < 1$ enable remarkable phenomena like superlensing, allowing imaging beyond the diffraction limit to achieve exceptionally high resolution. Importantly, although a RI below unity corresponds to superluminal phase velocities, this does not violate causality or special relativity, since the group velocity–which governs the actual transmission of information-remains limited by c.

4.1. Total reflection and scattering interpretation

The divergence of the effective potential $U(r)$ as $r \to r_0$ carries profound physical consequences for wave scattering. Near the throat, $f(r) \to 0$, and the dominant contribution to $U(r)$ arises from the terms proportional to $1/f(r)^2$ in the denominator of Eq. (46). This divergence creates an *infinite potential barrier* at the WH throat, which enforces total reflection of all incoming scalar wave modes, regardless of their frequency ω or angular quantum number m.

More precisely, defining the reflection coefficient $\mathcal{R}$ and transmission coefficient $\mathcal{T}$ for the Schrödinger-like problem (44), the infinite barrier height implies

$$|\mathcal{R}|^2 = 1, \qquad |\mathcal{T}|^2 = 0, \tag{50}$$

for all modes. This result stands in sharp contrast to BH spacetimes, where the event horizon acts as a perfectly absorbing boundary ($|\mathcal{T}|^2 > 0$), giving rise to finite greybody factors. The BSCWH geometry thus provides a concrete example of a gravitational configuration that scatters waves elastically, with the throat functioning as a perfect mirror.

While no net absorption occurs, the scattered waves acquire frequency-dependent phase shifts $\delta_m(\omega)$ that encode the full structure of the effective potential. These phase shifts can in principle be extracted from the asymptotic behavior of the scattered wave:

$$\chi(r) \xrightarrow{r\to\infty} A\,e^{i\omega r} + B\,e^{-i\omega r}, \qquad \text{with} \quad \frac{B}{A} = e^{2i\delta_m(\omega)}. \tag{51}$$

The phase shifts carry information about the WH throat geometry, the NS charge, and the disclination parameter, and could serve as observational discriminators between WH and BH spacetimes in the context of analogue gravity experiments.

The peak value $U_{\max}$ of the effective potential, attained at a radius $r_{\max}$ slightly above the throat, determines the characteristic frequency scale at which the transition from low-energy (strongly reflected) to high-energy (weakly perturbed) scattering occurs. In Table IV, we present $U_{\max}$ for various parameter combinations.

TABLE IV. Peak effective potential $U_{\max}$ and corresponding radius $r_{\max}$ for $b_0 = 1$, $\ell = 1$, and selected values of α, $\mathcal{Q}$, and m.

α	$\mathcal{Q}$	m	$r_{\max}$	$U_{\max}$
0.7	0.5	0	0.9830	112.5269
0.7	0.5	1	0.9830	114.6389
0.7	0.5	2	0.9830	120.9748
1.0	0.5	0	0.9830	112.5269
1.0	0.5	1	0.9830	113.5618
1.0	0.5	2	0.9830	116.6664
0.7	1.0	0	0.5500	247.1074
0.7	1.0	1	0.5500	253.8539
0.7	1.0	2	0.5500	274.0934
0.9	1.0	0	0.5500	247.1074
0.9	1.0	1	0.5500	251.1887
0.9	1.0	2	0.5500	263.4323
1.0	1.0	0	0.5500	247.1074
1.0	1.0	1	0.5500	250.4132
1.0	1.0	2	0.5500	260.3306

TABLE V. Effective RI $n(r)$ at selected radii for $b_0 = 1$, $\ell = 1$, $\mathcal{Q} = 1$, $m = 1$.

α	ω	$n(r=2)$	$n(r=3)$	$n(r=5)$	$n(r=10)$
0.7	1.5	0.889810	0.953983	0.983869	0.996008
0.7	2.0	0.939609	0.974383	0.990959	0.997756
0.7	3.0	0.973622	0.988697	0.995992	0.999003
0.8	1.5	0.919188	0.966283	0.988181	0.997074
0.8	2.0	0.955385	0.981177	0.993369	0.998355
0.8	3.0	0.980422	0.991678	0.997058	0.999269
0.9	1.5	0.938799	0.974627	0.991127	0.997805
0.9	2.0	0.966052	0.985808	0.995018	0.998766
0.9	3.0	0.985056	0.993718	0.997789	0.999452
1.0	1.5	0.952579	0.980552	0.993228	0.998327
1.0	2.0	0.973610	0.989107	0.996196	0.999059
1.0	3.0	0.988358	0.995174	0.998311	0.999582

As seen from the table, the potential peak increases sharply with $\mathcal{Q}$ (since larger charge shrinks the throat, concentrating curvature) and with m (reflecting the centrifugal barrier). Notably, for $m = 0$ the peak value $U_{\max}$ is *independent* of α, since the α^2 factors cancel identically in Eq. (47); the disclination affects only the m-dependent angular barrier contribution.

In Table V, we present numerical values of the effective RI at selected radial positions, quantifying the dispersive behavior.

The table confirms that $n(r) \to 1$ as $r \to \infty$ for all parameter combinations, and that the deviation from unity is most pronounced near the throat and for low frequencies, consistent with the dispersive analogue-gravity interpretation.

5. Conclusions

This study examined the optical properties-both ray-like and wave-like of a three-dimensional static charged BSCWH space-time incorporating topological disclinations. The objective was to understand how non-trivial geometric and topological features influenced the photon trajectories and scalar waves. The WH geometry was defined via a specific shape function $b(r)$, and the space-time incorporated a NS charge $\mathcal{Q}$ from string theory, along with a disclination parameter α that accounted for angular deficits due to topological defects. These components led to a non-asymptotically flat space-time exhibiting rich and complex optical behavior. The analysis of ray optics began with the study of NG motion. It was shown that both the disclination parameter α and the NS charge $\mathcal{Q}$ including the WH parameter b_0 significantly affected photon trajectories. The derived orbital equations and impact parameter relations, along with analytical expressions for the radial and angular evolution of light paths, show that photons experienced modified bending and shifting of trajectories, depending on the WH parameter b_0, the curvature scale ℓ, and the disclination parameter α.

A key finding in the ray-optics sector is the identification of the critical impact parameter $\beta_c = r_0$, which delineates scattered from traversing photon trajectories. We demonstrated that the trivial redshift function ($\Phi = 0$) inherent to the BSCWH geometry precludes the existence of a photon sphere, in contrast to standard BH spacetimes. This absence is a direct consequence of the metric structure and provides a potential observational signature for distinguishing BSCWH geometries from BH spacetimes. Furthermore, we derived the closed-form weak-field deflection angle (Eq. 36), which transparently separates the topological contribution $\pi(1-\alpha)/\alpha$ from the gravitational bending $b_0/(\alpha\beta)$ and the NS charge correction. This analytical result complements the exact elliptic integral expression and facilitates direct comparison with cosmic string lensing phenomenology [84].

The study then extended to wave optics by formulating the scalar Helmholtz equation in the curved space background and transforming it into a Schrödinger-like equation. This transformation allowed the identification of an effective potential $U(r)$, which depended on the disclination parameter, NS charge, and WH geometry. The resulting potential profiles showed that a decrease in α-indicating stronger topological defects-led to more localized and pronounced potentials. This suggested that disclinations enhanced wave localization and interference effects for scalar waves. Crucially, the divergence of $U(r)$ at the WH throat ($r \to r_0$) was shown to enforce total reflection of all scalar wave modes ($|\mathcal{R}|^2 = 1$), providing a clear wave-optics discriminator between WH and BH spacetimes: whereas BH horizons absorb incoming radiation (yielding finite greybody factors), the BSCWH throat acts as a perfect mirror, producing only frequency-dependent phase shifts (Table IV). In addition, we derived a frequency- and position-dependent effective RI $n(r)$ from the effective wave number $k_{\text{eff}}(r)$. The RI was found to depend not only on the radial coordinate r, but also on the wave frequency ω, the angular quantum number m, the curvature radius ℓ, the NS charge $\mathcal{Q}$, and the WH parameter b_0. This indicated a dispersive optical medium, wherein higher-frequency waves experienced stronger refractive effects, analogous to GL and optical phenomena in analogue gravity systems. Graphical analysis (see Figs. 7 to 8) and numerical tabulation (Tables V and IV) illustrated the behavior of the effective potential and RI under variations in α and ω, further confirming the influence of curvature and topological structure on wave propagation.

In summary, this investigation demonstrated the deep connection between spacetime geometry and the behavior of light in both classical and quantum regimes. It showed that topological features such as disclinations were not merely mathematical abstractions, but had measurable effects on wave and photon dynamics. These findings provided new insights into WH physics in lower-dimensional space-times and suggested potential applications in the design of analogue gravity systems and metamaterials, where engineered geometries could emulate such curved-space phenomena. In particular, the $n < 1$ RI profiles derived here share the characteristic features of metamaterial platforms studied in Refs. [69,70], while the disclination-induced lensing connects naturally to phonon transport in topological defect channels [68].

A natural direction for future work would be to extend the present analysis by considering more general classes of charged and rotating BSCWH geometries with topological defects, where the inclusion of angular momentum and higher-order curvature ($\mathcal{D}$) corrections could reveal richer optical behaviors. Also, test the influence of additional string-inspired fields, such as dilaton or Kalb-Ramond (KR) models, on photon trajectories and wave scattering, thereby connecting the optical properties of WHs with string theory frameworks. In this context, testing different types of perturbations, including electromagnetic and gravitational modes, could provide a broader illustration of how curvature (topological defect parameters) and disclinations affect wave propagation. Also, one could test the influence of the effective RI in GL models, especially its implications for distinguishing WH geometries from BH spacetimes. In this context, possible applications in analogue gravity platforms, such as metamaterials or optical lattices, may offer experimental realizations of the results, enabling the study of WH-inspired optics in controlled laboratory environments. Additionally, extending the wave-optics analysis to include quasinormal mode (QNM) calculations [17], electromagnetic perturbations, and the extraction of scattering phase shifts from the effective potential would provide a complete characterization of the BSCWH spectral fingerprint. The connection to holographic optics [90] and the recent developments in ray geodesics on curved surfaces [79] also merit further investigation.

Notes: Evaluation of the integral

We start with the integral

$$\Delta\phi = \int_{u_0}^{\infty} \frac{du}{\sqrt{\left(1 - b_0 u + \frac{\mathcal{Q}^2\ell^4}{4}u^2\right)(1-\beta^2 u^2)}}.$$

Define the quadratic polynomials

$$P(u) = 1 - b_0 u + \frac{\mathcal{Q}^2\ell^4}{4}u^2,$$

and

$$Q(u) = 1 - \beta^2 u^2.$$

The integral becomes

$$\Delta\phi = \int_{u_0}^{\infty} \frac{du}{\sqrt{P(u)Q(u)}}.$$

$$u_0 = \frac{2}{b_0 + \sqrt{b_0^2 - \mathcal{Q}^2\ell^4}},$$

The polynomial $P(u)$ is quadratic in u. Its roots are

$$\xi_{1,2} = \frac{b_0 \pm \sqrt{b_0^2 - \mathcal{Q}^2\ell^4}}{\frac{1}{2}\mathcal{Q}^2\ell^4}.$$

We rewrite

$$P(u) = \frac{\mathcal{Q}^2\ell^4}{4}(u-\xi_1)(u-\xi_2).$$

To bring the integral into a standard elliptic form, perform the substitution

$$u = \frac{1}{\beta}\sin\theta,$$

Computing du,

$$du = \frac{1}{\beta}\cos\theta d\theta.$$

The integrand denominator becomes

$$\sqrt{P(u)Q(u)} = \sqrt{P\left(\frac{\sin\theta}{\beta}\right)\left(1 - \beta^2\frac{\sin^2\theta}{\beta^2}\right)}$$
$$= \sqrt{P\left(\frac{\sin\theta}{\beta}\right)}\cos\theta.$$

Thus the integral is

$$\int \frac{\frac{1}{\beta}\cos\theta d\theta}{\cos\theta\sqrt{P\left(\frac{\sin\theta}{\beta}\right)}} = \frac{1}{\beta}\int \frac{d\theta}{\sqrt{P\left(\frac{\sin\theta}{\beta}\right)}}.$$

Substitute,

$$P\left(\frac{\sin\theta}{\beta}\right) = 1 - \frac{b_0}{\beta}\sin\theta + \frac{\mathcal{Q}^2\ell^4}{4\beta^2}\sin^2\theta.$$

Denote

$$A = 1, \quad B = -\frac{b_0}{\beta}, \quad C = \frac{\mathcal{Q}^2 \ell^4}{4\beta^2}.$$

So,

$$P\left(\frac{\sin\theta}{\beta}\right) = A + B\sin\theta + C\sin^2\theta$$
$$= C\,(\sin\theta - \beta\,\xi_1)\,(\sin\theta - \beta\,\xi_2).$$

Rewrite the integral as

$$I = \int \frac{d\theta}{\sqrt{A + B\sin\theta + C\sin^2\theta}}$$
$$= \int \frac{d\theta}{\sqrt{C\,(\sin\theta - \beta\,\xi_1)\,(\sin\theta - \beta\,\xi_2)}}.$$

This integral can be transformed into standard elliptic integrals by completing the square or using substitution.

The integral becomes

$$\Delta\phi = \frac{1}{\sqrt{-\beta^2 + \frac{\mathcal{Q}^2\ell^4}{4}}}\left[K(k) - F(\phi_0, k)\right],$$

where $K(k) = F(\pi/2, k)$ is the complete elliptic integral of the first kind, and $F(\phi_0, k)$ is the incomplete elliptic integral of the first kind.

Acknowledgments

The authors thank the Handling Editor, Prof. Ramón Castañeda Priego, and the anonymous Referees for their careful reading and constructive comments, which improved the manuscript. F.A. acknowledges the Inter University Centre for Astronomy and Astrophysics (IUCAA), Pune, India for granting visiting associateship. İ. S. expresses his thanks to TÜBİTAK, ANKOS, and SCOAP3 for their financial support. He further recognizes the backing of COST Actions CA22113, CA21106, CA23130, CA21136, and CA23115, which have played a important role in strengthening networking activities.

Data availability statement

No data associated in the manuscript.

1. L. Flamm, Beiträge zur Einsteinschen Gravitationstheorie, *Gen. Rel. Grav.* **47** (2015) 72, https://doi.org/10.1007/s10714-015-1908-2
2. A. Einstein and N. Rosen, The particle problem in the general theory of relativity, *Phys. Rev.* **48** (1935) 73, https://doi.org/10.1103/PhysRev.48.73
3. H. G. Ellis, Ether flow through a drainhole: A particle model in general relativity, *J. Math. Phys.* **14** (1973) 104, https://doi.org/10.1063/1.1666161
4. K. A. Bronnikov, Scalar-tensor theory and scalar charge, *Acta Phys. Pol. B* **4** (1973) 251.
5. J. A. Wheeler, Geometrodynamics (Academic Press, New York, 1962).
6. S. W. Hawking, Wormholes in spacetime, *Phys. Rev. D* **37** (1988) 904, https://doi.org/10.1103/PhysRevD.37.904
7. M. S. Morris and K. S. Thorne, Wormholes in spacetime and their use for interstellar travel, *Am. J. Phys*. **56** (1988) 395, https://doi.org/10.1119/1.15620
8. K. A. Bronnikov and A. M. Galiakhmetov, Wormholes without Exotic Matter in Einstein-Cartan Theory, *Gravit. Cosmol.* **21** (2015) 283, https://doi.org/10.1134/S0202289315040027
9. M. S. Churilova *et al.*, Wormholes without Exotic Matter: Quasinormal Modes, Echoes and Shadows, *JCAP* **2021** (2021) 010, https://doi.org/10.1088/1475-7516/2021/10/010
10. N. Godani and G. C. Samanta, Traversable wormholes in f(R) gravity, *New Astron.* **84** (2021) 101534, https://doi.org/10.1016/j.newast.2020.101534
11. M. S. Morris, K. S. Thorne, and U. Yurtsever, Wormholes, time machines, and the weak energy condition, *Phys. Rev. Lett.* **61** (1988) 1446, https://doi.org/10.1103/PhysRevLett.61.1446
12. J. P. S. Lemos and F. S. N. Lobo, Plane symmetric traversable wormholes in an anti-de Sitter background, *Phys. Rev. D* **69** (2004) 104007, https://doi.org/10.1103/PhysRevD.69.104007
13. M. Visser, Lorentzian Wormholes: From Einstein to Hawking (American Institute of Physics, Melville, NY, 1995), https://link.springer.com/book/9781563966538.
14. H. Huang and J. Yang, Charged Ellis Wormhole and Black Bounce, *Phys. Rev. D* **100** (2019) 124063, https://doi.org/10.1103/PhysRevD.100.124063
15. K. A. Bronnikov and M. S. Chernakova, Charged black holes and unusual wormholes in scalar-tensor gravity, *Grav. Cosmol.* **13** (2007) 51, https://doi.org/10.48550/arXiv.gr-qc/0703107
16. G. I. Róis *et al.*, Novel electrically charged wormhole, black hole and black bounce exact solutions in hybrid metric-Palatini gravity, *Phys. Rev. D* **111** (2025) 124012, https://doi.org/10.1103/PhysRevD.111.124012
17. G.-Y. Wu, S.-Y. Wang, and Y.-G. Miao, Perturbations of Einstein-Maxwell-phantom spacetime: instabilities of charged Ellis-Bronnikov wormholes and quasinormal modes of black holes, *Class. Quantum Grav.* **43** (2026) 015004, https://doi.org/10.1088/1361-6382/ae2733

18. L. Bixano and T. Matos, Possibility of the existence of wormholes in nature, *Phys. Rev. D* **113** (2026) 084004, https://doi.org/10.1103/mnkg-8ccb
19. L. Bixano and T. Matos, Einstein-Maxwell-dilaton wormholes that meet the energy conditions, *Phys. Rev. D* **111** (2025) 084056, https://doi.org/10.1103/PhysRevD.111.084056
20. L. Bixano, I. A. Sarmiento-Alvarado, and T. Matos, A brief review of wormhole cosmic censorship, *Axioms* **14** (2025) 831, https://doi.org/10.3390/axioms14110831
21. G. Miranda, J. C. Del Águila, and T. Matos, Exact rotating magnetic traversable wormholes satisfying the energy conditions, *Phys. Rev. D* **99** (2019) 124045, https://doi.org/10.1103/PhysRevD.99.124045
22. G. Clément and D. Gal'tsov, Rotating traversable wormholes in Einstein-Maxwell theory, *Phys. Lett. B* **838** (2023) 137677, https://doi.org/10.1016/j.physletb.2023.137677
23. G. Clément, D. Gal'tsov, and M. Guenouche, NUT wormholes, *Phys. Rev. D* **93** (2016) 024048, https://doi.org/10.1103/PhysRevD.93.024048
24. R. Ibadov, *et al.*, Scalarized nutty wormholes, *Symmetry* **13** (2021) 89, https://doi.org/10.3390/sym13010089
25. T. Matos and D. Nunez, Rotating scalar field wormhole, *Class. Quant. Grav.* **23** (2006) 4485, https://doi.org/10.1088/0264-9381/23/13/012
26. A. Ashraf *et al.*, Imprints of Quantum Gravity on Periastron Precession and Trajectories around a Black Hole, *Phys. Dark Universe* **47** (2025) 101787, https://doi.org/10.1016/j.dark.2024.101787
27. G. Mustafa *et al.*, Orbital Motion and Epicyclic Oscillations Around a Black Hole with Magnetic Charge, *Phys. Dark Universe* **47** (2025) 101765, https://doi.org/10.1016/j.dark.2024.101765
28. G. Mustafa *et al.*, Epicyclic Oscillations Around Slowly Rotating Charged Black Hole in Bumblebee Gravity, *Phys. Dark Universe* **47** (2025) 101753, https://doi.org/10.1016/j.dark.2024.101753
29. A. Ashraf *et al.*, Orbital Motion and QPOs Testing Around Rotating Hairy Black Holes in Horndeski Gravity, *Phys. Dark Universe* **47** (2025) 101725, https://doi.org/10.1016/j.dark.2024.101725
30. A. Ashraf *et al.*, Plasma Lensing, Epicyclic Oscillations, Particle Collision, and Thermal Fluctuations Around a Short-Hairy Black Hole, *Phys. Dark Universe* **48** (2025) 101836, https://doi.org/10.1016/j.dark.2025.101836
31. A. Ashraf *et al.*, Thermal Fluctuations, Particle Collision, QPOs, and Emission Energy Around a Schwarzschild Black Hole Immersed in Dehnen-Type Dark Matter Halo, *Phys. Dark Universe* **47** (2025) 101823, https://doi.org/10.1016/j.dark.2025.101823
32. A. Ditta *et al.*, Impact of Gravitational Collapse Exhibiting Loop Quantum Black Holes on Thermodynamical Features and Weak Gravitational Lensing, *Phys. Dark Universe* **47** (2025) 101818, https://doi.org/10.1016/j.dark.2025.101818
33. A. Ditta *et al.*, Particle Motion, Shadows and Thermodynamics of Regular Black Hole in Pure Gravity, *Phys. Dark Universe* **47** (2025) 101573, https://doi.org/10.1016/j.dark.2024.101573
34. A. Bouzenada *et al.*, Barrow Entropy Effects on Thermodynamics and Quasi-Periodic Oscillations Around a Frolov Black Hole, *Nucl. Phys. B* **1017** (2025) 116928, https://doi.org/10.1016/j.nuclphysb.2025.116928
35. A. Saleem *et al.*, Epicyclic Oscillations, Particle Collisions, Emission Energy and Thermal Fluctuation Around a Black Hole with de-Sitter Core, Nucl. Phys. B **1017** (2025) 116926, https://doi.org/10.1016/j.nuclphysb.2025.116926
36. R. Gregory and R. Laflamme, Black strings and p-branes are unstable, *Phys. Rev. Lett.* **70** (1993) 2837, https://doi.org/10.1103/PhysRevLett.70.2837
37. R. Gregory and R. Laflamme, The Instability of Charged Black Strings and p-Branes, *Nucl. Phys. B* **428** (1994) 399, https://doi.org/10.1016/0550-3213(94)90241-0
38. F. R. Tangherlini, Schwarzschild field in n dimensions and the dimensionality of space problem, *Nuovo Cim.* **27** (1963) 636, https://doi.org/10.1007/BF02784569
39. B. Kol, The Phase Transition Between Caged Black Holes and Black Strings, *Phys. Rep.* **422** (2006) 119, https://doi.org/10.1016/j.physrep.2005.09.003
40. T. Harmark and N. A. Obers, Phases of Kaluza-Klein Black Holes, *Class. Quantum Grav.* **21** (2004) 1709, https://doi.org/10.1088/0264-9381/21/7/013
41. P. Bostock and S. F. Ross, Smeared Branes and the Gubser-Mitra Conjecture, *Phys. Rev. D* **70** (2004) 064014, https://doi.org/10.1103/PhysRevD.70.064014
42. O. Aharony *et al.*, Black Hole-Black String Phase Transitions in Thermal 1 + 1-Dimensional Supersymmetric Yang-Mills Theory on a Circle, *Class. Quantum Grav*. **21** (2004) 5169, https://doi.org/10.1088/0264-9381/21/22/001
43. T. Harmark and N. A. Obers, New Phases of Near-Extremal Branes on a Circle, *JHEP* **2024** (2004) 022, https://doi.org/10.1088/1126-6708/2004/09/022
44. N. Arkani-Hamed, S. Dimopoulos, and G. Dvali, The Hierarchy Problem and New Dimensions at a Millimeter, *Phys. Lett. B* **429** (1998) 263, https://doi.org/10.1016/S0370-2693(98)00466-3
45. I. Antoniadis *et al.*, New Dimensions at a Millimeter to a Fermi and Superstrings at a TeV, *Phys. Lett. B* **436** (1998) 257, https://doi.org/10.1016/S0370-2693(98)00860-0
46. L. Randall and R. Sundrum, A Large Mass Hierarchy from a Small Extra Dimension, *Phys. Rev. Lett*. **83** (1999) 3370, https://doi.org/10.1103/PhysRevLett.83.3370
47. L. Randall and R. Sundrum, An Alternative to Compactification, *Phys. Rev. Lett*. **83** (1999) 4690, https://doi.org/10.1103/PhysRevLett.83.4690

48. M. Sharif and M. Azam, Stability Analysis of Thin- Shell Wormholes from Charged Black String, *JCAP* **2013** (2013) 023, https://doi.org/10.1088/1475-7516/2013/04/023

49. G. Alencar, T. M. Crispim, and F. S. N. Lobo (2025), https://doi.org/10.48550/arXiv.2505.04633.

50. A. Giacomini *et al*., Charged Black Strings and Black Branes in Lovelock Theories, *Phys. Rev. D* **98** (2018) 044019, https://doi.org/10.1103/PhysRevD.98.044019

51. A. S. Miranda *et al*., Separable Wave Equations for Gravitoelectromagnetic Perturbations of Rotating Charged Black Strings, Class. Quantum Grav. **32** (2015) 235002, https://doi.org/10.1088/0264-9381/32/23/235002

52. P. Goulart, Massless black holes and charged wormholes in string theory (2017), https://doi.org/10.48550/arXiv.1611.03164

53. S. E. Gralla and A. Lupsasca, Lensing by Kerr Black Holes, *Phys. Rev. D* **101** (2020) 044031, https://doi.org/10.1103/PhysRevD.101.044031

54. Y. Nambu, S. Noda, and Y. Sakai, Wave Optics in Black Hole Spacetimes, *Phys. Rev. D* **100** (2019) 064037, https://doi.org/10.1103/PhysRevD.100.064037

55. J. A. H. Futterman, F. A. Handler, and R. A. Matzner, Scattering from Black Holes (Cambridge University Press, 2009).

56. Event Horizon Telescope Collaboration, First M87 Event Horizon Telescope Results. I. The Shadow of the Supermassive Black Hole, Astrophys. *J Lett*. **875** (2019) L1, https://doi.org/10.3847/2041-8213/ab0ec7

57. F. S. N. Lobo, Exotic Solutions in General Relativity: Traversable Wormholes and Warp Drive Spacetimes, *Class. Quantum Grav.* **25** (2008) 175006, https://doi.org/10.1088/0264-9381/25/17/175006

58. F. Ahmed, Three-dimensional wormhole with cosmic string effects on eigenvalue solution of non-relativistic quantum particles, *Sci. Rep.* **13** (2023) 12953, https://doi.org/10.1038/s41598-023-40066-z

59. J. R. Muñoz de Nova, K. Golubkov, and J. Steinhauer, Observation of Thermal Hawking Radiation and Its Temperature in an Analogue Black Hole, *Nature* **569** (2019) 688, https://doi.org/10.1038/s41586-019-1241-0

60. W. Xiao, S. Tao, and H. Chen, Mimicking the gravitational effect with gradient index lenses in geometrical optics, *Photonics Research* **9** (2021) 1197, https://doi.org/10.1364/PRJ.418787

61. C. Sheng *et al*., Trapping light by mimicking gravitational lensing, *Nat. Photonics* **7** (2013) 902, https://doi.org/10.1038/nphoton.2013.247

62. T. Rojjanason, P. Burikham, and K. Pimsamarn, Charged fermion in 1 + 2-dimensional wormhole with axial magnetic field, *Eur. Phys. J. C* **79** (2019) 660, https://doi.org/10.1140/epjc/s10052-019-7156-y

63. S. Batz and U. Peschel, Linear and Nonlinear Optics in Curved Space: The Helmholtz Equation, *Phys. Rev. A* **78** (2008) 043821, https://doi.org/10.1103/PhysRevA.78.043821

64. A. Libster-Hershko, R. Shiloh, and A. Arie, Surface plasmon polaritons on curved surfaces, *Optica* **6** (2019) 115, https://doi.org/10.1364/OPTICA.6.000115

65. G. Della Valle *et al*., Experimental Observation of Optical Analogues of Gravitational Effects, *Phys. Rev. Lett.* **102** (2009) 180402, https://doi.org/10.1103/PhysRevLett.102.180402

66. R. Bekenstein *et al*., Optical Analogues of Gravitational Phenomena in Structured Media, *Phys. Rev. X* **4** (2014) 011038, https://doi.org/10.1103/PhysRevX.4.011038

67. D. Wang *et al*., Wave dynamics on toroidal surface, *Opt. Express* **26** (2018) 17820, https://doi.org/10.1364/OE.26.017820

68. S. Fumeron *et al*., Geometrical optics limit of phonon transport in a channel of disclinations, *Eur. Phys. J. B* **90** (2017) 95, https://doi.org/10.1140/epjb/e2017-70384-5

69. I. I. Smolyaninov, Linear and nonlinear optics of surface plasmon toy-models of black holes and wormholes, *Phys. Rev. B* **69** (2004) 205417, https://doi.org/10.1103/PhysRevB.69.205417

70. A. C. Hamilton and J. Courtial, Metamaterials for light rays: ray optics without wave-optical analog in the ray-optics limit, *New J. Phys.* **11** (2009) 013042, https://doi.org/10.1088/1367-2630/11/1/013042

71. S. Trettel, Classical Optics for Charged Black Holes (2025), https://doi.org/10.48550/arXiv.2505.04633.

72. M. Çalışkan *et al*., Probing Wave-Optics Effects and Low-Mass Dark Matter Halos with Lensing of Gravitational Waves from Massive Black Holes (2023), https://doi.org/10.1103/PhysRevD.108.123543.

73. F. dos S. Azevedo *et al*., An Optical Wormhole from Hollow Disclinations, *Phys. Rev. A* **103** (2021) 023516, https://doi.org/10.1103/PhysRevA.103.023516

74. C. Xu and L.-G.Wang, Theory of light propagation in arbitrary two-dimensional curved space, *Photonics Res.* **9** (2021) 2486, https://doi.org/10.1364/PRJ.435993

75. Z. Shao and Z. Wang, Propagation and transformation of a light beam on a curved surface, *Optics Express* **29** (2021) 8626, https://doi.org/10.1364/OE.416997

76. S. Gurtas Dogan, A. Guvendi, and O. Mustafa, Ray Trajectories and Wave Optics in a Traversable Wormhole: Optics of a Minimal Surface, *Nucl. Phys. B* **1018** (2025) 117000, https://doi.org/10.1016/j.nuclphysb.2025.117000

77. S. G. Dogan, A. Guvendi, and O. Mustafa, Ray and wave optics in an optical wormhole, *Phys. Lett. B* **868** (2025) 139626, https://doi.org/10.1016/j.physletb.2025.139626

78. S. G. Dogan, O. Mustafa, and A. Guvendi, Ray and wave optics in Bonnor-Melvin domain walls: Photon rings, *Nucl. Phys.* B **1016** (2025) 116920, https://doi.org/10.1016/j.nuclphysb.2025.116920

79. S. Gurtas Dogan, A. Guvendi, and O. Mustafa, Ray Geodesics and Wave Propagation on the Beltrami Surface: Optics of an Optical Wormhole, *Eur. Phys. J C* **85** (2025) 896, https://doi.org/10.1140/epjc/s10052-025-14644-6

80. F. Ahmed and A. Bouzenada, Geometric and wave optics in a topologically charged Perry-Mann type wormhole with disclinations, *Phys. Lett. B* **868** (2025) 139704, https://doi.org/10.1016/j.physletb.2025.139704

81. F. Ahmed and A. Bouzenada, Ray and wave dynamics in a static FRW spacetime with conical singularity, *Phys. Lett. B* **868** (2025) 139743, https://doi.org/10.1016/j.physletb.2025.139743

82. G. P. Perry and R. B. Mann, Traversable Wormholes in (2+1) Dimensions, *Gen. Relativ. Gravit.* **24** (1992) 305, https://doi.org/10.1007/BF00760244

83. W. T. Kim, J. J. Oh, and M. S. Yoon, Charged Black String and Kaluza-Klein Bubble, *Phys. Rev. D* **70** (2004) 044006, https://doi.org/10.1103/PhysRevD.70.044006

84. J. R. Gott, III, Gravitational lensing effects of vacuum strings: Exact solutions, Astrophys. J. (United States) **288** (1985) 422

85. W. A. Hiscock, Exact Gravitational Field of a String, *Phys. Rev. D* **31** (1985) 3288, https://doi.org/10.1103/PhysRevD.31.3288

86. B. Linet, The Static Metrics with Cylindrical Symmetry Describing a Model of Cosmic Strings, *Gen. Relativ. Gravit.* **17** (1985) 1109, https://doi.org/10.1007/BF00774195

87. F. Ahmed, I. Sakallı, and A. Al-Badawi, Gravitational lensing phenomena of Ellis-Bronnikov-Morris-Thorne wormhole with global monopole and cosmic string, *Phys. Lett. B* **864** (2025) 139448, https://doi.org/10.1016/j.physletb.2025.139448

88. M. Abramowitz and I. A. Stegun, Handbook of Mathematical Functions With Formulas, Graphs, and Mathematical Tables, Applied Mathematics Series (United States Government Printing Office, Washington D.C., 1972).

89. I. S. Gradshtein and I. M. Ryzhik, Table of Integrals, Series, and Products (Academic Press, 2007), https://doi.org/10.1016/C2010-0-64839-5.

90. P. Phukon and T. Sarkar, f(R)-Charged Black Holes and Holographic Optics, *JHEP* **2013** (2013) 102, https://doi.org/10.1007/JHEP09(2013)102